

Coupling thermal evolution of planets and hydrodynamic atmospheric escape in MESA

Daria Kubyshkina,¹[★] Aline A. Vidotto,¹ Luca Fossati² and Eoin Farrell¹

¹*School of Physics, Trinity College Dublin, the University of Dublin, College Green, Dublin-2, Ireland*

²*Space Research Institute, Austrian Academy of Sciences, Schmiedlstrasse 6, A-8042 Graz, Austria*

Accepted XXX. Received YYY; in original form ZZZ

ABSTRACT

The long-term evolution of hydrogen-dominated atmospheres of sub-Neptune-like planets is mostly controlled by two factors: a slow dissipation of the gravitational energy acquired at the formation (known as thermal evolution) and atmospheric mass loss. Here, we use MESA to self-consistently couple the thermal evolution model of lower atmospheres with a realistic hydrodynamical atmospheric evaporation prescription. To outline the main features of such coupling, we simulate planets with a range of core masses ($5\text{--}20M_{\oplus}$) and initial atmospheric mass fractions (0.5–30%), orbiting a solar-like star at 0.1 au. In addition to our computed evolutionary tracks, we also study the stability of planetary atmospheres, showing that the atmospheres of light planets can be completely removed within 1 Gyr, and that compact atmospheres have a better survival rate. From a detailed comparison between our results and the output of the previous-generation models, we show that coupling between thermal evolution and atmospheric evaporation considerably affects the thermal state of atmospheres for low-mass planets and, consequently, changes the relationship between atmospheric mass fraction and planetary parameters. We, therefore, conclude that self-consistent consideration of the thermal evolution and atmospheric evaporation is of crucial importance for evolutionary modeling and a better characterization of planetary atmospheres. From our simulations, we derive an analytical expression between planetary radius and atmospheric mass fraction at different ages. In particular, we find that, for a given observed planetary radius, the predicted atmospheric mass fraction changes as $age^{0.11}$.

Key words: Hydrodynamics – Planets and satellites: atmospheres – Planets and satellites: physical evolution

1 INTRODUCTION

The evolution of planetary atmospheres is a complex topic, which requires multiple considerations, including the formation of planetary systems from the circumstellar disks (e.g., Mizuno 1980; Morbidelli et al. 2009; Morbidelli & Raymond 2016; Morbidelli 2020; Mordasini et al. 2012; Leconte et al. 2015), the possible migration of planets (e.g., Mordasini et al. 2015; Morbidelli & Raymond 2016; Morbidelli 2020), and the atmospheric accretion (e.g., Ikoma & Hori 2012; Stökl et al. 2015, 2016). It then proceeds with the thermal evolution of the atmosphere (e.g., Rogers & Seager 2010; Nettelmann et al. 2011; Miller & Fortney 2011; Valencia et al. 2013; Lopez et al. 2012; Lopez & Fortney

2014), the removal of primordial atmospheres due to atmospheric escape processes (e.g., Watson et al. 1981; Lammer et al. 2003, 2016; Erkaev et al. 2007, 2016; Lecavelier des Etangs et al. 2004; Salz et al. 2016; Kubyshkina et al. 2018a), including the joint evolution of the host star (e.g., Sanz-Forcada et al. 2011; Wright et al. 2011; Jackson et al. 2012; Shkolnik & Barman 2014; McDonald et al. 2019). Accurately combining these ingredients is key for explaining the existing population of exoplanets, as revealed by observations (e.g. Bonfils et al. 2013; Mullally et al. 2015), and unveiling the history of planetary formation and their co-evolution with host stars. As the evolution of planetary atmospheres is driven to a large extent by stellar irradiation, the study of this evolution can also provide the information needed to constrain the past evolution of stars hosting planetary systems (Kubyshkina et al. 2019a,b; Owen & Campos Estrada

[★] E-mail: kubyshkd@tcd.ie

2020). In turn, constraining the stellar evolution (particularly at young ages, when stars are known to follow various paths in terms of their high energy luminosity, see e.g. Tu et al. 2015) is one of the first and necessary steps in habitability studies (e.g., Lammer et al. 2018, 2019).

An accurate modelling of atmospheric evolution is also important for characterisation of exoplanets and interpretation of observations. Recent missions, such as Transiting Exoplanet Survey Satellite (TESS; Ricker et al. 2015) and CHaracterising ExOPlanets Satellite (CHEOPS; Broeg et al. 2013), are dedicated to study exoplanets and can provide an outstanding level of measurement precision, which calls for finer analysis tools.

In this work, we concentrate on the thermal evolution of the primordial atmospheres of sub-Neptune planets. For that, we use MESA (Modules for Experiments in Stellar Astrophysics, Paxton et al. 2018), coupled with atmospheric mass loss. The evolution of planetary atmospheres has been studied with MESA before (e.g., Ikoma & Hori 2012; Lopez et al. 2012; Lopez & Fortney 2013; Stökl et al. 2016), and the escaping atmosphere was modelled using an energy limited approximation (e.g., Watson et al. 1981; Erkaev et al. 2007). This approximation, however, has been shown to be inappropriate for the study of sub-Neptune size planets (Stökl et al. 2016; Lammer et al. 2016; Owen & Wu 2016; Fossati et al. 2017; Kubyskhina et al. 2018a). The novelty of our work here is that we combine the study of the thermal evolution with the more realistic prescription for atmospheric mass loss from hydrodynamical studies (Kubyskhina et al. 2018a,b). Our method allows us to investigate how those processes interact with each other and how much escape can affect planetary evolution.

An accurate prescription of atmospheric mass loss is of crucial importance in the study of atmospheric evolution. A proper coupling of the thermal evolution with atmospheric escape is relevant for calculating the actual atmospheric mass fraction from mass and radius measurements.

We consider sub-Neptune-like planets in the planetary mass range of 5-20 Earth masses with initial atmospheric mass fractions between 0.5 and 30% orbiting a Solar-like star at the orbital separation of 0.1 AU. These planets are highly affected by atmospheric escape, making them a good sample for investigation of the possible effects of coupling between atmospheric escape and thermal evolution.

This paper is organised as follows. In Section 2 we describe our modelling approach. In Section 3 we present our results and compare how the evolution is affected when assuming different atmospheric mass loss prescriptions (the simplified energy limited approach or the more robust hydrodynamic prescription). Further, in Section 4, we consider the relation between atmospheric mass fraction and planetary parameters throughout the evolution. We discuss our results and give the conclusions in Section 5.

2 MODELLING APPROACH: COUPLING HYDRODYNAMICAL ESCAPE SIMULATIONS INTO MESA

The ‘Modules for Experiments in Stellar Astrophysics’ (MESA) (Paxton et al. 2011, 2013, 2018) is a widely used tool in Stellar Physics, having a wide range of

applications in the field of stellar evolution and internal structure (e.g., Cantiello et al. 2014; Choi et al. 2016; Marchant et al. 2016; Farrell et al. 2020a,b). An interesting, but less common use of MESA, is that of modelling the thermal evolution of giant or sub-Neptune planets (see e.g. Batygin & Stevenson 2013; Storch & Lai 2014; Nayakshin 2015; Jackson et al. 2016; Chen & Rogers 2016; Dederick & Jackiewicz 2017; Berardo & Cumming 2017; Chatterjee & Chen 2018; Malsky & Rogers 2020). Here we describe how we use MESA to simulate the evolution of sub-Neptune planets. To describe such low-mass objects, MESA employs the equation of state (EOS) from Saumon et al. (1995) (SCVH EOS in MESA documentation) and use opacity tables from Freedman et al. (2008) (further details on the use of MESA for planetary modelling can be found in Paxton et al. 2013).

2.1 Initial conditions

In this work, we employ the MESA version 12115 (Paxton et al. 2018) to model the thermal evolution of sub-Neptune planets in the mass range between 5 and 20 Earth masses (M_{\oplus}). To set up the planets, which we further evolve, we follow the basic algorithm suggested by Chen & Rogers (2016), which we describe here briefly.

(i) At the first step, we create a coreless planet of 0.1 Jupiter masses using `create_initial_model` (alternatively, one can use the initial model from the test suite available in MESA directory (`test_suite/irradiated_planet/0.001Msun.mod`) and reduce its mass using `relax_initial_mass`).

(ii) Next, we insert an inert core¹ of the specific mass (5, 7.5, 10, 12.5, 15, and 20 M_{\oplus}) using the `relax_core` option, hence modify the internal boundary condition. Here, we adopt the bulk density of the core given by Rogers et al. (2011) for the rocky composition.

(iii) We reduce the atmosphere to the desired volume using `relax_initial_mass`. For each of the cores from the previous step we consider atmospheric mass fractions of 0.5, 1, 2, 3, 5, 10, 20, and 30%.

(iv) Further, we standardize the initial energy budget of the planet. We set an artificial luminosity with `relax_initial_L_center` option as described in Chen & Rogers (2016) to inflate the atmosphere, and then evolve the planet without atmospheric escape for 5 Myr, which is an average lifetime of protoplanetary discs (Mamajek 2009).

(v) At the final step, we remove the artificial luminosity and set up an initial temperature at the upper boundary of 772 K using `relax_initial_irradiation` option. This temperature corresponds to the equilibrium temperature assuming zero albedo of a planet orbiting at 0.1 AU around a solar mass star at the age of 5 Myr (resolved from the stellar parameters given by MESA Isochrones and Stellar Tracks; MIST Choi et al. 2016).

After these steps, the newborn planet is ready to evolve.

¹ In the present paper, ‘core’ is the solid part of the planet composed of silicates and metals, and we do not take into account its internal structure.

2.2 Thermal evolution and atmospheric escape

To further account for the atmospheric heating by the host star irradiation, we create a user routine using the `other_energy` module of MESA, which tracks the equilibrium temperature of the atmosphere during the evolution as resolved using MIST. This is different to the approach of [Chen & Rogers \(2016\)](#), who assumed a constant temperature (compatible with the present Sun) throughout the evolution of the planet. We will discuss the implications from this update in the next section. We also include in the heating function the time-dependent luminosity of the core, accounting for its thermal inertia and radiogenic heating ([Chen & Rogers 2016](#)).

The most important novelty of our work relates to the treatment of atmospheric escape. For that, we use the results of hydrodynamical (HD) simulations of atmospheric escape presented by [Kubyshkina et al. \(2018a\)](#). These models consider a pure hydrogen atmosphere and describe atmospheric heating by absorption of the stellar XUV (x-ray+extreme ultraviolet) flux; they account for hydrogen dissociation, recombination, and ionization, and $Ly\alpha$ - and H_3^+ -cooling. The grid of models in [Kubyshkina et al. \(2018a\)](#) consists of about 7000 models and covers planetary mass (M_{pl}) in the range of 1 – 40 M_{\oplus} , planetary radius (R_{pl}) in the range of 1-10 R_{\oplus} , orbital separations corresponding to equilibrium temperatures (T_{eq}) between 300 and 2000 K, stellar masses between 0.4 and 1.3 M_{\odot} , and stellar irradiation levels from the present Sun (scaled to the specific stellar masses) to about 10^4 times solar (appropriate for younger stars).

Given that escape depends on the properties of the planet (mass, radius, orbital separation) and of the star (age, XUV radiation), it would have been computationally intensive to run one model for each timestep of the MESA simulation. To overcome this, we use the semi-analytic approach described in [Kubyshkina et al. \(2018b\)](#). This analytical approximation is based on the large grid of hydrodynamical 1D models of planetary upper atmospheres (described above) and is very convenient for incorporating in planetary evolution studies. The analytical description has as arguments the planetary radius, mass and temperature, orbital separation and stellar flux and is given by

$$\dot{M}_{\text{HBA}} = e^{\beta} (F_{\text{XUV}})^{\alpha_1} \left(\frac{d_0}{\text{AU}} \right)^{\alpha_2} \left(\frac{R_{\text{pl}}}{R_{\oplus}} \right)^{\alpha_3} \Lambda^{\kappa}, \quad (1)$$

$$\kappa = \zeta + \theta \ln \left(\frac{d_0}{\text{AU}} \right), \quad (2)$$

where coefficients α_1 , α_2 , α_3 , β , ζ , and θ are given in Table 1 of [Kubyshkina et al. \(2018b\)](#). Hereafter, we refer to this analytical approximation as the hydro-based approximation (HBA).

To compare the results of our novel model with previous work, we also consider the energy limited approximation, in which the escape rate is given as

$$\dot{M}_{\text{EL}} = \frac{\pi \eta R_{\text{pl}} R_{\text{XUV}}^2 F_{\text{XUV}}}{G M_{\text{pl}} K}, \quad (3)$$

where the factor K accounts for Roche-lobe effects ([Erkaev et al. 2007](#)) and η is the fraction of the incoming energy that is used in the heating process. To be consistent with assumptions of the hydrodynamic models, we adopt here $\eta = 15\%$. Following [Chen & Rogers \(2016\)](#), we assume

the absorption radius of the stellar XUV radiation in Equation 3 to be

$$R_{\text{XUV}} = R_{\text{pl}} + H \ln \left(\frac{P_{\text{photo}}}{P_{\text{XUV}}} \right), \quad (4)$$

where R_{pl} is the photospheric radius of the planet, H and P_{photo} are the atmospheric scale height and the pressure at the photosphere, respectively. The pressure at the XUV absorption level is defined as $P_{\text{XUV}} \approx (m_{\text{H}} G M_{\text{pl}}) / (\sigma_{\nu_0} R_{\text{pl}}^2)$, where M_{pl} is the mass of the planet, G and m_{H} are the gravitational constant and the mass of hydrogen, respectively, and $\sigma_{\nu_0} = 1.89 \cdot 10^{-18} \text{ cm}^2$ is the absorption cross-section of hydrogen defined for the typical energy of the XUV radiation of 20 eV. Despite Equation 4 being a simplification, the effective radii of XUV absorption defined this way are similar to those obtained through HD simulations (see Figure A1).

To describe the time-dependent stellar flux ($\text{erg s}^{-1} \text{ cm}^{-2}$) at the planetary orbit we use the power law

$$F_{\text{XUV}} = \begin{cases} 29.7 \left(\frac{\text{age}}{1 \text{ Gyr}} \right)^{-1.23} \left(\frac{d_0}{\text{AU}} \right)^{-2}, & \text{if age} > t_{\text{sat}} \\ 886 \left(\frac{d_0}{\text{AU}} \right)^{-2}, & \text{if age} \leq t_{\text{sat}} \end{cases} \quad (5)$$

where d_0 is the orbital separation of the planet and t_{sat} is the time until which the star remains in the saturated regime (e.g., [Wright et al. 2011](#); [Tu et al. 2015](#); [McDonald et al. 2019](#)). We introduced the latter, as we start our simulation at a very young age, when the power law in the first line of Equation 5 ([Ribas et al. 2005](#)) gives the unrealistically high XUV levels. To avoid it, we set the saturation level for $L_{\text{X}}/L_{\text{bol}}$ at the typical for near-solar mass stars value of 2×10^{-4} ([McDonald et al. 2019](#); [Jackson et al. 2012](#)). Taking the average L_{bol} at first 100 Myr of evolution of 2.9×10^{33} (about 0.74 of the present Sun level; based on MIST [Choi et al. 2016](#)), we obtain L_{X} at the saturation stage of $5.8 \times 10^{29} \text{ erg/s}$, which we further convert into $F_{\text{XUV}} = 8.86 \times 10^4 \text{ erg/(s} \cdot \text{cm}^2)$ at the orbital separation of 0.1 AU (see [Sanz-Forcada et al. 2011](#), for the conversion relation). The saturation time for the considered case is therefore slightly less than 100 Myr.

The MESA inlists and supplement functions used in the present work are publicly available in Zenodo Repository (<https://doi.org/10.5281/zenodo.4022393>)².

3 COMPARISON BETWEEN RADIATION HYDRODYNAMICS MODEL AND ENERGY-LIMITED APPROXIMATION FOR ATMOSPHERIC LOSS

3.1 The case of the 12.5 M_{\oplus} core model

Before describing the results for the whole set of planets considered in this work, we discuss a typical example of the evolutionary tracks for the planet with a core mass of 12.5 M_{\oplus} and an initial atmospheric mass fraction of 20% (the total mass of the planet at the beginning of the simulation is therefore $M_{\text{pl},0} = M_{\text{core}} / (1 - \frac{f_{\text{at},0}}{100\%}) = 15.63 M_{\oplus}$), to introduce some

² Using the inlists available at the MESA market one may need to apply a handful of minor corrections to comply with the most recent releases of MESA. The present work is based on version 12115.

of the main features of our results. In Figure 1 (top panel), we present the atmospheric escape rates (\dot{M}) throughout the evolution for HBA (red line) and energy-limited (black) prescriptions, denoting the duration of the saturation period of the host star by the vertical dashed-dotted line. One can see, that two mass loss mechanisms give significantly different outputs at the beginning of the evolution, when the atmosphere of the planet is hot and inflated. This period is relatively short: about 60 Myr for the considered case. Afterwards, the two mass loss prescriptions predict similar escape rates. This means, that most of the effect to the final mass-radius distribution caused by the choice of the mass loss prescription is decided during this short period after the protoplanetary disk dispersal. We note that the duration of this period does not always coincide with the saturation time as it happens for the planet in Figure 1; this period is shorter for the lighter planets, as their atmospheres are experiencing stronger escape, and their radii are therefore decreasing fast, thus increasing the planetary gravity. This higher gravity reduces the mass loss rate, thus extending the timescale for the survival of the atmosphere. The differences in mass loss rates are in general higher for lighter planets, including for the later stages in evolution.

In the bottom panel of Figure 1 we present the evolution of the planetary radius, including the case of a purely thermal evolution in the absence of atmospheric escape (gray line). The shape of the evolutionary track in the energy limited case (black line) is mainly governed by the thermal evolution of the planet, with atmospheric escape gradually decreasing the radius of the planet. The bump at ~ 30 Myr pairs with the heating of the atmosphere shown in the equilibrium temperature profile in the inset plot in the top panel. As we can see in Figure 1, the final radii of the planet at 5 Gyr is very different depending on the assumption made for the atmospheric escape. While the energy limit is an improvement related to the case where no escape is considered, the models using the energy-limited approximation still over-predict the size of the planet, compared to the more realistic escape model using radiation hydrodynamics.

As we noted in the introduction, one additional difference between our models and those by [Chen & Rogers \(2016\)](#) lies on the treatment of the temperature of the planet. While in their models they assume the planet remains at the same equilibrium temperature throughout the evolution, in our models, we use a stellar evolutionary track to derive the stellar bolometric luminosity and thus the equilibrium temperature of the planet (inset in the top panel of Figure 1). We find that the evolutionary tracks in case of the energy limited atmospheric escape are nearly unaffected by considering a time-dependent equilibrium temperature. However, for the HBA model, the difference can be significant – up to $\sim 20\%$ in terms of radii for the considered set of planets. This can be explained by the fact that the equilibrium (photospheric) temperature is not part of Equation 3 and affects the \dot{M}_{EL} indirectly only through the variation of the planetary radius. In the case of the HBA models (Equation 1), this temperature is accounted for through the orbital separation (for details see [Kubyskhina et al. 2018a,b](#)), and the gravitational parameter of the planet Λ .

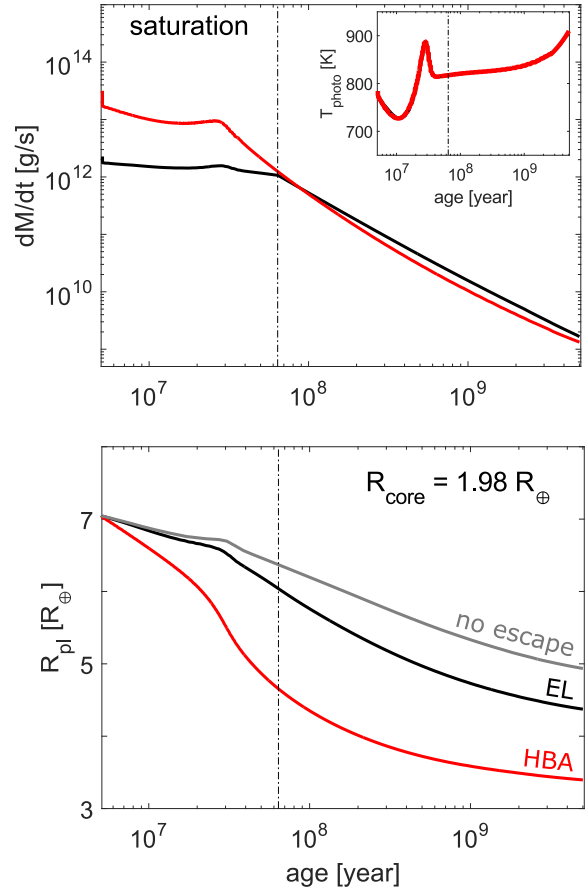


Figure 1. Evolutionary tracks of the atmospheric mass loss rate (top panel) and radius of the planet (bottom panel) considering different mass loss prescriptions: hydrodynamic models (HBA, red lines) and energy limited approximation (black lines). The gray line in the bottom panel shows how the radius of the planet changes in the absence of atmospheric escape, i.e., solely due to thermal evolution. The vertical dashed-dotted lines denote the end of the period when the star remains in the saturation regime. With the additional sub-plot in the top panel we show how the photosphere (equilibrium) temperature changes with time to illustrate the adopted model of stellar heating.

3.2 Evolution for different core masses and initial atmosphere sizes

As a result of what shown above, for different atmospheric mass loss prescriptions, the distributions of atmospheric mass fractions and planetary radii against planetary core masses look different throughout the evolution. In Figure 2, we show the mass-radius diagram of the planet at the ages of 10 Myr, 100 Myr, and 5 Gyr. Here, the red solid lines correspond to the HBA mass loss prescription, and the black dashed lines correspond to the energy-limited prescription; lines with different symbol sizes correspond to the different initial atmospheric mass fractions (from 1% to 30% for lines from top to bottom within each panel). Similar to what was shown in the example above, the mass loss rates for these two prescriptions differ dramatically in the first tens of Myr for the lighter planets in the sample to ~ 100 Myr for the heav-

ier ones; the difference itself is particularly large for lower gravity and highly inflated planets (i.e., those having a large initial envelope, see the case of 30% initial atmosphere). Despite this period being relatively short, it basically defines the final state of the planet, and therefore the difference in planetary radii predicted by the two different mass loss prescriptions remains nearly the same from 100 Myr to 5 Gyr. One can notice that some of the symbols present in the top panel (10 Myr) are missing in the two bottom panels for the cases of escaping atmospheres. This occurs due to the complete loss of the atmosphere taking place before 100 Myr (see, e.g., the $5 M_{\oplus}$ planet for the HBA prescription in red) or before 5 Gyr (e.g., the $7.5 M_{\oplus}$ planet and HBA atmospheric mass loss).

The third set of curves we show in Figure 2 is given by the grey lines - these curves represent the cases where no escape is considered throughout the evolution of the planet. This means that the size of the planet evolves with time only due to the thermal evolution of their atmospheres. Similarly to what we exemplified in Figure 1, not considering escape over-predicts the final sizes of the planets.

Considering the HBA mass loss prescription (red curves in Figure 2), one can see that the planets with core masses below $10 M_{\oplus}$ end up with the same radii independently of the initial size of their atmospheres (except for the most compact initial atmospheres, see the case of $f_{\text{at},0} = 1\%$). Although these planets start their evolution with different radii, depending on their initial f_{at} , after a few tens of Myr, we see that their ‘final’ radii converged to the same value and changed only slightly for the rest of their lifetime. This effect is caused by the following: when increasing the amount of atmosphere for a low-mass planet at the formation stage, the radius increases significantly (this is seen well at the radius distribution in absence of mass loss, grey lines in Figure 2, top panel), while the total mass of the planet changes only slightly, as the atmosphere is the minor part of the total mass of the planet. The HBA atmospheric escape rate depends on the planetary radius to more than a power of 3 in the “low gravity” regime (which is usually the case for the young planets). As a result, after the amount of atmosphere reaches some critical value (which is $\sim 5\%$ and $\sim 10\%$ for the planets of 7.5 and $10 M_{\oplus}$ core masses considered here, respectively), the further increase in radius leads to a consequent increase of the atmospheric mass loss rate. This effect was considered in details in [Kubyshkina et al. \(2019a\)](#).

3.3 Survival timescales of atmospheres

In Figure 3, we present the atmospheric escape timescale τ at 10 and 100 Myr against the initial atmospheric mass fraction $f_{\text{at},0}$. This parameter

$$\tau = M_{\text{atm}}/\dot{M}$$

represents the instantaneous time that is needed to fully remove an atmosphere of mass M_{atm} if the mass loss rate \dot{M} remained constant. The larger the value of τ , the larger is the survival chance of the atmosphere. As most of the atmospheric losses occur at the early stages of evolution, we consider the parameter τ for 10 and 100 Myr only in Figure 3. The different line colors in Figure 3 represent different masses of planetary cores (increasing from the bottom to the

top); solid lines correspond to the HBA prescription, and dashed lines correspond to the energy-limited prescription.

Both mass loss prescriptions predict similar dependencies: the longest timescales peaks at relatively compact initial envelopes. However, the survival chance decreases steeply towards the smallest atmospheres, and it also decreases towards the largest one, because at some point the increase in escape rate overcomes the increase in the mass of the atmosphere. Nevertheless, a closer analysis reveals some differences between the two escape approaches. The HBA predicts larger survival timescales for the smaller envelopes compared to the energy-limited approximation (τ maximizes at $f_{\text{at},0} \sim 1 - 2\%$ compared to $3 - 10\%$ for the energy limited approach). Also, for HBA, the maximum is more clearly pronounced and the shape of the curve remains similar for all planetary core masses in the considered interval, while for the energy-limited approach the maximum in τ is more pronounced for the lighter planets. The only exception for the shape of $\tau(f_{\text{at},0})$ -dependence in case of HBA is the flattening of the curves at low masses and large initial envelopes, which is caused by the existence of the “critical” size of the atmosphere discussed above (which is about 5% for the $7.5 M_{\oplus}$ planet, and about 10% for the $10 M_{\oplus}$ planet considered here).

To further illustrate an increase in survival chances for the mid-compact atmospheres, we show in Figure 4 the distribution of the atmospheric mass fractions against the planetary core masses of our simulated planets at the age of 5 Gyr. The different lines represent different initial atmospheric mass fractions; the color code shows the relation of instant atmospheric mass (at 5 Gyr) to the initial one ($\frac{f_{\text{at}}}{f_{\text{at},0}}$). For all considered core masses, the atmospheres started as compact ones preserve the largest part of initial masses compare to very thin or highly inflated ones.

For $10 M_{\oplus}$ core, however, not more than 10% of initial envelope is preserved in any of the cases. This makes a lucky combination of the parameters important for the survival of the atmosphere around such planet if it was exposed to the stronger irradiation from the host star (e.g. if it would orbit closer in).

4 RELATION BETWEEN PLANETARY RADII AND ATMOSPHERIC MASS FRACTION

Through observations, we can constrain the radii and masses of exoplanets. Ideally, we would like to find a relationship between $\{M_{\text{pl}}, R_{\text{pl}}\}$ and atmospheric mass fraction from our models. Therefore, once $\{M_{\text{pl}}, R_{\text{pl}}\}$ are observationally derived (provided we know the system’s age), we can infer some physical properties for the planetary atmosphere. In this section, we explore the possibility of finding a relation between planetary radii and atmospheric mass fraction (hereafter, $f_{\text{at}} \times R_{\text{pl}}$ -relation).

4.1 Basic trends in thermal evolution

In this Section, we aim to study the behavior of the $f_{\text{at}} \times R_{\text{pl}}$ -relation depending on the system parameters (as age and planetary mass) for the given set of simulated planets. Figure 5 shows with small symbols all the planets we modeled with ages between 10 Myr and 5 Gyr (color coded). It is

interesting to see that at each age, and for each considered mass these points lie roughly along one line, which is well fitted by a cubic polynomial (solid lines in Figure 5). We give the coefficients of the cubic fits in the Appendix B.

We note from Figure 5 that the value of f_{at} for a specific radius is larger for older systems. We can also see that the line curvature increases, becoming more convex at older ages. From this, we infer that the shape of this line is controlled by the thermal evolution of the planet (including the input from stellar heating). For each planetary mass (with various initial atmosphere masses) this line can be approximated by a cubic polynomial with a mean squared error of 10^{-6} – 10^{-7} . This can be useful, for example, when one derives the radius of the planet from observations and would like to estimate its atmospheric mass fraction. Therefore, the evolution of the $f_{\text{at}} \times R_{\text{pl}}$ -relation of an individual planet can be considered as the sum of two processes: change of the $f_{\text{at}} \times R_{\text{pl}}$ curve with time due to thermal evolution, and the movement of the planet along this curve towards smaller radii due to atmospheric escape, where the speed of this movement is defined by the mass loss prescription. We illustrate this process in Figure 5 for the $12.5 M_{\oplus}$ planet with $f_{\text{at},0} = 10\%$: the position of the planet at each moment in time is shown by the large circles.

In Figure 6 (top panel) we show how the cubic polynomial approximation of $f_{\text{at}} \times R_{\text{pl}}$ we obtained for the $12.5 M_{\oplus}$ planet changes with age for different radii between 2.5 and $7 R_{\oplus}$ (from bottom to top). Each of the considered radii corresponds to smaller f_{at} at earlier ages, due to higher temperatures. One can see that $f_{\text{at,approx}}(\text{age})$ is nearly linear in the logarithm space; it means we can estimate the power law that describes this relation. Averaging among the different masses in our data set, we obtain

$$f_{\text{at,approx}} \propto \left(\frac{\text{age}}{1 \text{ Gyr}} \right)^{0.11}, \quad (6)$$

for each considered radii and where the proportionality constant is different for each R_{pl} . Equation 6 remains valid also in case of non-escaping atmospheres, which means that this trend is general for the thermal evolution and is weakly affected by differences in the thermal state of the planet caused by the escape (although the proportionality constant changes for different escape mechanisms).

The dependence of the f_{at} given by the cubic polynomial approximation on the planetary mass (see Figure 6, bottom panel) is less simple. For the lowest atmospheric mass fractions, the radius of the planet (which can be considered as a sum of core radius and thickness of the atmosphere) depends strongly on the mass-dependent core size of the planet. This results in a negative correlation between f_{at} and planetary mass ($f_{\text{at}} \propto M_{\text{pl}}^{-0.5}$) for $f_{\text{at}} \lesssim 10\%$. For $f_{\text{at}} \sim 15\%$, $f_{\text{at}} \times R_{\text{pl}}$ is nearly constant with mass, while for larger $f_{\text{at}} \gtrsim 15\%$, we see a positive trend with mass, changing from $\propto M_{\text{pl}}^{0.1}$ to $\propto M_{\text{pl}}^{0.25}$, for f_{at} from 15 to 30%, respectively. This difference in $f_{\text{at,approx}}(M_{\text{pl}})$ dependence reflects the change in the thermal evolution of the planet due to atmospheric escape: since the thermal state of low mass planets is the most affected (while the heaviest planet in the simulation set is nearly not affected), the contrast in the $f_{\text{at}} \times R_{\text{pl}}$ -relation between low and high planetary masses increases with inclusion of atmospheric mass loss. This confirms our inference that the self-

consistent inclusion of the thermal evolution and realistic atmospheric escape is relevant for the evolution of low-mass planets.

4.2 Comparison of the $f_{\text{at}} \times R_{\text{pl}}$ -relation with models that do not self-consistently account for escape and thermal evolution

Lopez & Fortney (2014) showed that, due to the thermal evolution of the atmosphere, the relation between atmospheric mass fraction and planetary radius can not be uniquely defined from the measurable parameters of the planet, such as planetary mass and equilibrium temperature. In fact, the $f_{\text{at}} \times R_{\text{pl}}$ -relation also depends on the age of the planet (i.e., on the current state of its thermal evolution), and the dependence on age is stronger than the dependence on the incident XUV flux from the star. The inclusion of atmospheric escape can complicate the situation even more, as escape is coupled with thermal evolution: loss of the atmosphere speeds up the cooling of the planet, and, in turn, the cooling of the planet and consequent shrinking the radius reduce mass loss. From our simulations, the difference in temperature at the bottom of the atmosphere after 5 Gyr reaches up to 3000 K, when comparing cases with HBA escape and when escape is neglected. The largest temperature differences are for the smallest planetary masses and largest atmospheric mass fractions, while for heavy planets with compact atmospheres they can be insignificant (e.g., for the $20 M_{\oplus}$ planet and $f_{\text{at},0} \lesssim 10\%$ the difference in temperature at the bottom of the atmosphere does not exceed 200 K).

In Figure 7, we consider how the $f_{\text{at}} \times R_{\text{pl}}$ -relation changes due to mass loss for the case of the planet with the core mass of $12.5 M_{\oplus}$, and with the initial atmospheric mass fraction of $f_{\text{at},0} = 20\%$. Here, the black solid line represents the relation obtained in the present framework, i.e., MESA combined with HBA prescription for the mass loss. The black dashed line shows the evolution using MESA, but now assuming the energy limited mass loss mechanisms. One can see, that despite the same starting point, the two tracks look different, and therefore if, for the energy-limited approach an atmosphere of $f_{\text{at}} \sim 15\%$ is reached at an age of 5 Gyr when the radius is $\sim 4.4 R_{\oplus}$, for HBA the same atmospheric mass fraction is reached at an age below 100 Myr, when the radius of the planet is $\sim 6 R_{\oplus}$.

Therefore, similarly to what was concluded by Lopez & Fortney (2014), these different radii for a specific amount of atmosphere are achieved at different moments in the evolution and, thus, at different thermal states of the atmosphere. From the observer's point of view, this means that by measuring the radius of the planet, without knowledge of its age, one can not derive the amount of atmosphere the planet has.

4.2.1 Comparison using the $12.5 M_{\oplus}$ -core planet

In addition to the faster/slower transition between thermal states due to the specific atmospheric escape mechanism, the thermal state at each given time can be altered due to the coupling of thermal evolution with atmospheric mass loss. In order to separate and quantify the effects of these two processes individually, we consider three additional $f_{\text{at}} \times R_{\text{pl}}$

tracks. For these tracks, we couple the HBA prescription of atmospheric mass loss to three semi-analytical prescriptions between atmospheric mass fraction and planetary radius that have been adopted in the literature. We assume starting parameters of the planet equivalent to those with which we start the MESA run. Next, we calculate the atmospheric mass loss rate with HBA, define the appropriate time step (requiring not more than 0.5% of the whole atmosphere to be lost within one step), and infer the atmospheric mass accordingly. Then we estimate the new radius of the planet from the new atmospheric mass fraction and adjusted parameters of the system. We repeat this process until we reach the final time of 5 Gyr or the atmosphere is totally gone. We vary the incident flux from the star and the temperature at the photosphere throughout the evolution in the same way as for MESA runs. The detailed description of this approach can be found in [Kubyshkina et al. \(2018a, 2019a\)](#). Note that, contrary to our study performed with MESA in which escape is self-consistently coupled to the thermal evolution of planets, the use of semi-analytical $f_{\text{at}} \times R_{\text{pl}}$ -relations plus the prescription of escape is not self-consistent.

As a first $f_{\text{at}} \times R_{\text{pl}}$ prescription, we employ the analytical approximation given in [Lopez & Fortney \(2014\)](#). Their model considers the thermal evolution of the planetary atmosphere in absence of mass loss and employs a similar approach as MESA, including the same EOS and opacity tables; the time-dependent luminosity of the core in this model follows the approach of [Lopez et al. \(2012\)](#) and is the same as in the present work. Most of the difference with respect to the approach in this paper comes therefore from the boundary and starting conditions. The $f_{\text{at}} \times R_{\text{pl}}$ -relations derived by [Lopez & Fortney \(2014\)](#) and our MESA model without atmospheric escape have the similar shape throughout the evolution, but the former predicts an atmospheric mass that is smaller by less than 30% (within our set of simulated planets) than the latter. Therefore, adding atmospheric escape to [Lopez & Fortney \(2014\)](#), see the Lopez+HBA model in Figure 7 (dotted light blue line), leads to a similar systematic shift in atmospheric mass to our $f_{\text{at}} \times R_{\text{pl}}$ -relation (black solid line).

[Lopez & Fortney \(2014\)](#) considered the planetary radius R_{pl} as the sum of the core radius ($R_{\text{core}}/R_{\oplus} \approx (M_{\text{pl}}/M_{\oplus})^{0.25}$) and the radius of the convective hydrogen-helium dominated envelope (R_{env}), and the radius of the radiative upper part ($R_{\text{atm}} \approx 9k_{\text{b}}T_{\text{eq}}/(g\mu_{\text{H/He}})$), where the latter is estimated assuming the pressure at the photosphere of 20 mbar and at the radiative-convective boundary of 100 mbar. R_{env} is given by the analytical approximation based on 1300 thermal evolution models and depend on the planetary mass, atmospheric mass fraction, incident stellar flux and age of the planet.

As the photosphere in our MESA runs is defined in a different way and normally lies at a lower altitude than that given at 20 mbar, we consider in addition to the total R_{pl} given by this approximation (light blue dotted line in Figure 7), the reduced value of ($R_{\text{core}} + R_{\text{env}}$) only, which gives on average about 10% smaller radii than the “full radius” model (dark blue dotted line). Comparing the general properties of “full radius” and “reduced radius” model (i.e., without R_{atm}), we see that the inclusion of R_{atm} on the top of convective zone barely changes the atmospheric mass for this specific planet. This is because the removed upper layers have low atmo-

spheric density. However, the radius changes considerably and is about 10-15% lower for the “reduced radius” models shown in Figure 7, when comparing models at the same age. The pressures at the upper boundary for the “full radius” model and for the “reduced radius” model are 20 mbar and 100 mbar, respectively. The pressure at the upper boundary given by MESA is in general between these values for the planets considered in this paper (in particular, for the planet considered in this section it remains ~ 76 mbar throughout the evolution). Therefore, if the coupling between thermal evolution and atmospheric escape is of minor importance, we expect the planetary radius given by MESA for the specific planetary parameters to lie in between these two estimations for most of the cases (except for the lightest planets in the present set, where the radii at the young ages are strongly affected by the hotter start in [Lopez & Fortney 2014](#)). However, as one can see in Figure 7, for the $12.5M_{\oplus}$ -core planet, this remains true only for the first ~ 100 Myr, presumably due to the inclusion of mass loss. This behaviour is similar for the other planets in our framework, and we investigate this in more detail in Section 4.2.2.

At last, we consider the estimation of the atmospheric mass fraction given by the model of [Johnstone et al. \(2015a\)](#) (violet line in Figure 7). This model is based on the TAPIR (The AdaPtive, Implicit RHD) code developed by [Stökl et al. \(2015\)](#), which provides radiative hydrodynamical models for the atmospheres of planets with a given mass, radius and equilibrium temperature. The nebula-accreted atmosphere in this case is considered to be in hydrostatic and thermal equilibria, and the luminosity of the core (established at the formation) is the main heating source. The model employs the EOS by [Saumon et al. \(1995\)](#), gas opacities by [Freedman et al. \(2008\)](#) and dust opacities by [Semenov et al. \(2003\)](#). As this model is initially intended to describe the atmospheres newly accreted from the protoplanetary disk, its natural upper boundary is the Hill radius. For the estimates of the atmospheric mass fractions we define the photospheric pressure as in [Kubyshkina et al. \(2018a\)](#). We exploit the grid of atmosphere models given by this approach covering the same range of planetary parameters as the grid of upper atmosphere models ([Kubyshkina et al. 2018a](#)) used to construct HBA, and interpolate within this grid to estimate the atmospheric mass fractions.

Though this model employs the same EOS and the same gas opacities as MESA, there are several differences in the modelling approaches. For the planet considered in Figure 7, this model gives an estimate similar to the one given by the present model (compare violet and solid black lines). The difference in the atmospheric masses for the given radius throughout the evolution remains on average about $0.04M_{\text{pl}}$ (i.e., about 20% of the initial envelope). The S-shaped variation in the middle of the track corresponds to the variation in the stellar temperature (and therefore, heating of the planet) predicted by MIST. The temperature gradient in the model of [Stökl et al. \(2015\)](#); [Johnstone et al. \(2015a\)](#) is determined from radiative transport whereas in MESA, the temperature gradient is found by combining radiative transport with mixing-length theory. As a result, the different treatments makes the atmosphere more sensitive to heat variations in the model of [Stökl et al. \(2015\)](#); [Johnstone et al. \(2015a\)](#). This model also does not account for the thermal evolution

of the planet, so in general the difference of this estimate to the results of MESA+HBA is expected to be the largest.

Overall, for all semi-analytical prescriptions, the resulting radii at the end of the evolution are similar to those given by the self-consistent modelling of the thermal evolution and atmospheric mass loss (within $\sim 20\%$ uncertainty), but the corresponding atmospheric mass fractions can differ significantly. All the models shown in Figure 7 predict a final radius of $\sim 3\text{--}3.4 R_{\oplus}$, but the atmospheric mass fraction ranges from 0.025 to 0.06 M_{pl} . Next, we perform the same comparison for all simulated planets in our sample.

4.2.2 Comparison for all planets

For all of the simulated planets considered in this work we see a similar behavior to what we saw in the case of the $12.5 M_{\oplus}$ -core planet. Differences in f_{at} increase with age for the approaches of Johnstone et al. (2015a) (violet) and Lopez & Fortney (2014) with “full radius” (light blue) up to about 10 times (with an average increase of 2.5 times), while for the approach of Lopez & Fortney (2014) with “reduced radius” (dark blue), f_{at} decreases from $\Delta f_{\text{at}} \approx 10\text{--}100\% f_{\text{at}}$ to $\Delta f_{\text{at}} \approx 4\text{--}20\% f_{\text{at}}$. The differences in f_{at} given for a specific R_{pl} by different approaches increase with age by one order of magnitude for all three prescriptions for $f_{\text{at}} \lesssim 1\%$; also, the difference given by the approximation of Johnstone et al. (2015a) (not accounting for the thermal evolution) increases relative to the others, while for the first ~ 100 Myr they remain at the same average level.

We summarize the difference between models for all our simulated planets in Figure 8, where we plot the relative difference in the atmospheric mass ($100\% \times \Delta f_{\text{at}}/f_{\text{at}}$) given by the semi-analytical approaches to the one given by MESA+HBA. The color coding remains the same as in Figure 7. We consider this distribution at 5 Gyr for two reasons. First, the difference in the thermal state of the planet for the models considering and not considering mass loss reaches its maximum at the end of simulation, therefore, these discrepancies can be considered as upper limits. Second, this allows one to minimize the implicit difference in $f_{\text{at}} \times R_{\text{pl}}$ through time caused by the different starting conditions in Lopez & Fortney (2014) compared to our approach (they assume the hotter start, i.e., the initial entropy of the atmosphere is slightly higher).

Considering the four different modelling approaches at 5 Gyr, for $f_{\text{at}} \gtrsim 2\%$, for most of the simulated planets the absolute value of $\Delta f_{\text{at}}/f_{\text{at}}$ varies between 4 and 70%, where the upper limit is outlined by the approximation of Johnstone et al. (2015a) (magenta points). Overall, the discrepancies of Johnstone et al. (2015a) with our reference model are larger than those of other models, but they remain at a similar level at different ages, which can make it a better approximation for the most compact atmospheres, since systematic differences are easier to correct.

Because the differences between our coupled model (MESA+HBA) and the three other approximations are usually below 70% for $f_{\text{atm}} \gtrsim 2\%$, these four approximations give acceptable estimates of $f_{\text{at}} \times R_{\text{pl}}$ at 5 Gyr. However, if one requires a detailed characterisation of the planet, we conclude that treating the thermal evolution of the planet self-consistently with the hydrodynamical modelling of at-

mospheric escape should be considered, in particular for the low mass planets.

5 DISCUSSION AND CONCLUSIONS

Here, we modelled the long-term evolution of sub-Neptune planets orbiting solar-like stars. Our models considered planets with a range of core and atmospheric masses. We used MESA to model the thermal evolution of planetary atmospheres and self-consistently included atmospheric escape in our simulations. MESA has been used before to study planetary evolution, but the novelty of our work is that we used the more realistic prescription for atmospheric escape from hydrodynamical studies (Kubyskhina et al. 2018a,b). In particular, we incorporated the ‘hydro-based approximation’ (HBA, Equations 1), which is an analytical approximation from grids of escape models, into MESA. Our inlists and supplement functions can be accessed from the MESA market.

We found that the relation between the atmospheric mass fraction and the radius of the planet is controlled to a large extent by the thermal state of the atmosphere, which changes with time as the planet cools down after formation, and can be significantly affected by atmospheric escape. For the set of planets considered in here, we found that the difference in temperature at the bottom of the atmosphere for the escaping and non-escaping atmospheres can reach a few thousand kelvin after 5 Gyr. This implies that atmospheric escape changes the thermal gradient in the atmosphere, with the effect being larger for the smaller planetary masses with expanded atmospheres. In turn, the variations in the thermal state of the planet (and therefore, the radius) affects the escape rate. This implies that an accurate and self-consistent prescription of atmospheric mass loss is of crucial importance in the study of atmospheric evolution, in particular for low mass (below $\sim 15 M_{\oplus}$) planets.

Despite the differences caused by atmospheric escape, there are some general trends that are similar for the cases of escaping and non-escaping atmospheres. In both cases, the atmospheric mass fraction corresponding to a specific planetary radius changes with time as $\text{age}^{0.11}$. The dependence on planetary mass retains qualitatively the same behaviour in both cases as well; however, quantitatively it differs more for low planetary masses and atmospheric mass fractions above $\sim 10\%$.

There has been other studies that self-consistently incorporated escape in MESA (e.g., Chen & Rogers 2016), albeit using a different prescription for planetary mass loss than the HBA. To compare with previous works, we also simulated thermal evolution of planets using the commonly adopted energy limited (EL) approximation. Concerning the planetary evolution, the HBA prescription leads to higher chances of survival of the primary atmospheres for more compact planets, compared to what was obtained applying the EL approximation. Furthermore, the HBA prescription moves the boundary between old planets with and without a primary atmosphere towards higher mass planets.

We also compared our results with other models, such as that of Lopez & Fortney (2014), which considers a different thermal evolution model from that given by MESA without atmospheric escape, and that of Johnstone et al. (2015a),

which calculated atmospheric mass without accounting for thermal evolution. To make the comparison more adequate, we implemented the HBA mass loss on these models and compare their results with our MESA+HBA models. In all these cases, the planetary radii at the end of the simulation (5Gyr) are relatively similar, with a difference below 20%, to those predicted by the combination of MESA with HBA. The atmospheric mass fractions, however, show a difference of up to 70% compared to our models for planets with atmospheric mass fractions above 2%, and up to a few times for the lighter atmospheres. This can not be explained only by differences in the approaches used in the models, as the differences in $f_{\text{at}} \times R_{\text{pl}}$ relation grow systematically with age; therefore, the larger differences compared to the case of non-escaping atmospheres should come from the effect on the thermal evolution caused by atmospheric mass loss. From this, we concluded that, separately considering atmospheric escape and thermal evolution can yet be acceptable for rough estimates of planetary radii and atmospheric mass fraction for larger atmospheres, or for massive planets with relatively compact envelopes.

However, for an accurate modelling of the atmospheric escape or characterisation of observed exoplanets, the thermal evolution process and atmospheric escape should be considered self-consistently. Our findings show that the choice of a more realistic atmospheric mass loss prescription is crucial for evolutionary studies. New instrumentation, such as the CHEOPS satellite (Broeg et al. 2013), which are capable of measuring planetary radii to the 2-3% level, will provide the necessary accuracy enabling one to identify the effects of self-consistently accounting for both planetary thermal evolution and mass loss.

ACKNOWLEDGEMENTS

This project has received funding from the European Research Council (ERC) under the European Union's Horizon 2020 research and innovation programme (grant agreement No 817540, ASTROFLOW).

DATA AVAILABILITY

The data underlying this article are available in Zenodo Repository, at <https://doi.org/10.5281/zenodo.4022393>.

REFERENCES

- Batygin, K., & Stevenson, D. J. 2013, *ApJ*, 769, L9
 Berardo, D., & Cumming, A. 2017, *ApJ*, 846, L17
 Bonfils, X., Delfosse, X., Udry, S., et al. 2013, *A&A*, 549, A109
 Broeg, C., Fortier, A., Ehrenreich, D., et al. 2013, *European Physical Journal Web of Conferences*, 03005
 Cantello, M., Mankovich, C., Bildsten, L., et al. 2014, *ApJ*, 788, 1, id. 93
 Chatterjee, S., & Chen, H. 2018, *ApJ*, 852, 58
 Chen, H., & Rogers, L. A. 2016, *ApJ*, 831, 180
 Choi, J., Dotter, A., Conroy, C., et al. 2016, *ApJ*, 823, 102
 Cubillos, P., Harrington, J., Lored, T. J., et al. 2017, *AJ*, 153, 3
 Dederick, E., & Jackiewicz, J. 2017, *ApJ*, 837, 148
 Erkaev, N. V., Kulikov, Y. N., Lammer, H., et al. 2007, *A&A*, 472, 329
 Erkaev, N. V., Lammer, H., Odert, P., et al. 2016, *MNRAS*, 460, 1300
 Farrell, E. J., Groh, J. H., Meynet, G., and Eldridge, J. J. 2020, *MNRAS*, 494, 1, 53
 Farrell, E. J., Groh, J. H., Meynet, G., et al. 2020, *MNRAS*, 495, 4, 4659
 Fossati, L., Erkaev, N. V., Lammer, H., et al. 2017, *A&A*, 598, A90
 Freedman, R. S., Marley, M. S., & Lodders, K. 2008, *ApJS*, 174, 504
 Ikoma, M., & Hori, Y. 2012, *ApJ*, 753, 66
 Jackson, A. P., Davis, T. A., & Wheatley, P. J. 2012, *MNRAS*, 422, A24
 Jackson, B., Jensen, E., Peacock, S., et al. 2016, *Celestial Mechanics and Dynamical Astronomy*, 126, 227
 Jeans, J. 1925, *The Dynamical Theory of Gases*. By Sir James Jeans. Cambridge University Press, 1925. ISBN: 978-1-1080-0564-7
 Johnstone, C. P., Güdel, M., Stökl, A., et al. 2015, *ApJ*, 815, L12
 Kubyskhina, D., Fossati, L., Mustill, A. J., et al. 2019, *A&A*, 632, A65
 Kubyskhina, D., Cubillos, P., Fossati, L., et al. 2019, *ApJ*, 879, 1, 26
 Kubyskhina, D., Fossati, L., Erkaev, N. V., et al. 2018a, *A&A*, 619, A151
 Kubyskhina, D., Fossati, L., Erkaev, N. V., et al. 2018b, *ApJ*, 866, L18
 Lammer, H., Selsis, F., Ribas, I., et al. 2003, *ApJ*, 598, L121
 Lammer, H., Erkaev, N. V., Fossati, L., et al. 2016, *MNRAS*, 461, L62
 Lammer, H., Zerkle, A. L., Gebauer, S., et al. 2018, *A&ARv*, 26, 2
 Lammer, H., Sproß, L., Grenfell, J. L., et al. 2019, *Astrobiology*, 19, 927
 Lecavelier des Etangs et al. 418, L1, *A&A*2004
 Leconte, J., Forget, F., & Lammer, H. 2015, *Experimental Astronomy*, 40, 449
 Lopez, E. D., Fortney, J. J., & Miller, N. 2012, *ApJ*, 761, 59
 Lopez, E. D., & Fortney, J. J. 2013, *ApJ*, 776, 2
 Lopez, E. D., & Fortney, J. J. 2014, *ApJ*, 792, 1
 McDonald, G. D., Kreidberg, L., & Lopez, E. 2019, *ApJ*, 876, 22
 Mamajek, E. E. 2009, *American Institute of Physics Conference Series*, 1158, 3
 Malsky, I., & Rogers, L. A. 2020, *arXiv e-prints*, arXiv:2002.06466
 Marchant, P., Langer, N., Podsiadlowski, P., et al. 2016, *A&A*, 588, id.A50
 Miller, N., & Fortney, J. J. 2011, *ApJ*, 736, L29
 Mizuno, H. 1980, *Progress of Theoretical Physics*, 64, 544
 Morbidelli, A., Bottke, W. F., Nesvorný, D., et al. 2009, *Icarus*, 204, 558
 Morbidelli, A., & Raymond, S. N. 2016, *Journal of Geophysical Research (Planets)*, 121, 1962
 Morbidelli, A. 2020, *A&A*, 638, A1
 Mordasini, C., Alibert, Y., Klahr, H., et al. 2012, *A&A*, 547, A111
 Mordasini, C., Mollière, P., Dittkrist, K.-M., et al. 2015, *International Journal of Astrobiology*, 14, 201
 Mullally, F., Coughlin, J. L., Thompson, S. E., et al. 2015, *ApJS*, 217, 31
 Murray-Clay, R. A., Chiang, E. I., & Murray, N. 2009, *ApJ*, 693, 23
 Nayakshin, S. 2015, *MNRAS*, 454, 64
 Nettelmann, N., Fortney, J. J., Kramm, U., et al. 2011, *ApJ*, 733, 2
 Owen, J. E., & Wu, Y. 2016, *ApJ*, 817, 107
 Owen, J. E., & Wu, Y. 2017, *ApJ*, 847, 29
 Owen, J. E., & Lai, D. 2018, *MNRAS*, 479, 5012
 Owen, J. E., & Campos Estrada, B. 2020, *MNRAS*, 491, 5287
 Paxton, B., Bildsten, L., Dotter, A., et al. 2011, *ApJS*, 192, 3

- Paxton, B., Cantiello, M., Arras, P., et al. 2013, *ApJS*, 208, 4
- Paxton, B., Schwab, J., Bauer, E. B., et al. 2018, *ApJS*, 234, 34
- Pizzolato, N., Maggio, A., Micela, G., Sciortino, S., & Ventura, P. 2003, *A&A*, 397, 147
- Ribas, I., Guinan, E. F., Güdel, M., et al. 2005, *ApJ*, 622, 680
- Ricker, G. R., Winn, J. N., Vanderspek, R., et al. 2015, *Journal of Astronomical Telescopes, Instruments, and Systems*, 1, 014003
- Rogers, L. A., & Seager, S. 2010, *ApJ*, 712, 974
- Rogers, L. A., Bodenheimer, P., Lissauer, J. J., et al. 2011, *ApJ*, 738, 59
- Salz, M., Schneider, P. C., Czesla, S., & Schmitt, J. H. M. M. 2016, *A&A*, 585, L2
- Sanz-Forcada, J., Micela, G., Ribas, I., et al. 2011, *A&A*, 532, A6
- Saumon, D., Chabrier, G., & van Horn, H. M. 1995, *ApJS*, 99, 713
- Semenov, D., Henning, T., Helling, C., et al. 2003, *A&A*, 410, 611
- Shkolnik, E. L., & Barman, T. S. 2014, *AJ*, 148, 64
- Stökl, A., Dorfi, E., & Lammer, H. 2015, *A&A*, 576, A87
- Stökl, A., Dorfi, E. A., Johnstone, C. P., et al. 2016, *ApJ*, 825, 86
- Storch, N. I., & Lai, D. 2014, *MNRAS*, 438, 1526
- Tu, L., Johnstone, C. P., Güdel, M., & Lammer, H. 2015, *A&A*, 577, L3
- Valencia, D., Guillot, T., Parmentier, V., et al. 2013, *ApJ*, 775, 10
- Watson, A. J., Donahue, T. M., & Walker, J. C. G. 1981, *Icarus*, 48, 150
- Wright, N. J., Drake, J. J., Mamajek, E. E., & Henry, G. W. 2011, *ApJ*, 743, 48

APPENDIX A: EFFECTIVE RADII OF THE STELLAR XUV ABSORPTION.

Here we present the distribution of the effective radii of the stellar XUV absorption predicted by the Equation 4 for the planets in our data set in comparison to the predictions of HD models (Figure A1). The latter were obtained through the interpolation within the grid of upper atmosphere models presented in Kubyshkina et al. (2018a). The two estimates agree well for the gravitational parameters $\Lambda \gtrsim 15$.

APPENDIX B: CUBIC POLYNOMIAL FITS COEFFICIENTS

In Table B we present the coefficients of the cubic polynomial approximations of $f_{\text{at}} \times R_{\text{pl}}$ dependence for all the planetary core masses considered in this work at different moments in time. These coefficients are of the restricted use, as they are bound to the specific system configuration. They can, however, be used to test the general trends in $f_{\text{at}} \times R_{\text{pl}}$.

This paper has been typeset from a \LaTeX file prepared by the author.

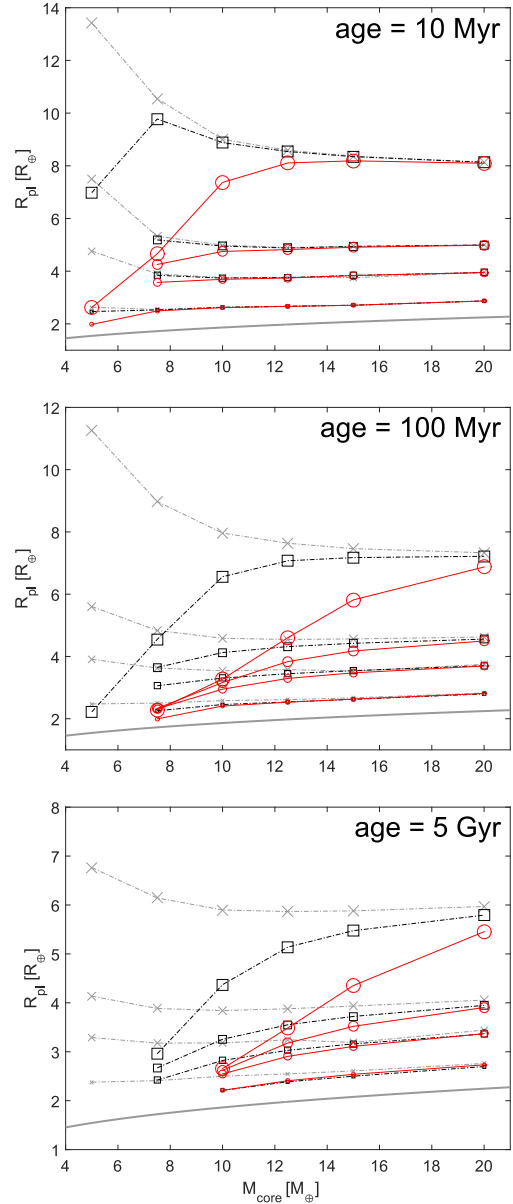


Figure 2. Mass-radius diagrams throughout the evolution at ages 10 Myr, 100 Myr, and 5 Gyr (from top to bottom panels). Black lines with square symbols correspond to the energy-limited atmospheric mass loss, red lines with circles to the hydrodynamic prescription (HBA), and the light gray lines with crosses correspond to the thermal evolution of the planet without mass loss. The size of symbols increases with initial atmospheric mass fractions, from bottom to top curves: 1, 5, 10, and 30%. Note that some of the points are omitted at the low mass range at 100 Myr and 5 Gyr due to the complete loss of the atmosphere. The gray solid lines represent the core radii accepted for the different planetary masses in this study (Rogers et al. 2011)

Table B1. Here we present the coefficients of the cubic polynomial approximation $f_{at} = c_0 + c_1 R_{pl} + c_2 R_{pl}^2 + c_3 R_{pl}^3$ for the set of planets simulated in the present work at different ages. Note that these coefficients are of the restricted use, as they are bound to the specific system configuration.

$M_{\text{core}} [M_{\oplus}]$	age [Myr]	c_0	c_1	c_2	c_3
7.5	6	-9.5174186e-02	3.7805986e-02	2.4897235e-03	-5.4846104e-05
7.5	10	-9.6726476e-03	-1.5654047e-02	1.1662104e-02	-5.5184314e-04
7.5	30	1.1613491e-02	-4.0110695e-02	1.9335906e-02	-1.2887226e-03
7.5	50	3.3928231e-02	-6.2786585e-02	2.6864042e-02	-2.0914725e-03
7.5	100	8.2414444e-02	-1.1580330e-01	4.5702243e-02	-4.2533551e-03
7.5	500	2.4745440e-01	-3.0179365e-01	1.1367423e-01	-1.2295493e-02
7.5	1000	2.3423878e-01	-2.8697032e-01	1.0822829e-01	-1.1659277e-02
7.5	5000	3.2817317e-01	-4.1002648e-01	1.6175864e-01	-1.9374941e-02
10	6	-8.4337932e-02	2.1263943e-02	7.2651128e-03	-2.5831732e-04
10	10	-1.1829657e-01	4.7280208e-02	1.2402145e-03	1.2094692e-04
10	30	-2.0784025e-02	-1.4012184e-02	1.2077970e-02	-5.2396709e-04
10	50	-8.2177727e-03	-2.6373716e-02	1.5658310e-02	-8.0826119e-04
10	100	-1.5884565e-02	-2.3379397e-02	1.5859988e-02	-8.8580159e-04
10	500	6.4912519e-02	-9.7909313e-02	3.7497361e-02	-2.7851885e-03
10	1000	1.0935944e-01	-1.3935513e-01	4.9605804e-02	-3.8843362e-03
10	5000	9.2015409e-02	-1.2035197e-01	4.2755580e-02	-3.1194446e-03
12.5	6	-1.0294407e-01	2.9212775e-02	6.0305936e-03	-1.3372028e-04
12.5	10	-9.8722962e-02	2.8063438e-02	5.8132746e-03	-1.2044831e-04
12.5	30	-8.9115448e-02	2.8857909e-02	3.5865897e-03	6.9361893e-05
12.5	50	-5.8511717e-02	8.4950426e-03	7.6332101e-03	-1.6251869e-04
12.5	100	-3.7070666e-02	-8.1771528e-03	1.1563853e-02	-4.2972074e-04
12.5	500	7.5268361e-03	-4.8910663e-02	2.2855972e-02	-1.3199504e-03
12.5	1000	4.7302452e-02	-8.2469558e-02	3.1634502e-02	-2.0195481e-03
12.5	5000	9.5876225e-02	-1.2094996e-01	4.1060868e-02	-2.7550134e-03
15	6	-1.1683502e-01	3.9591844e-02	2.7564329e-03	1.6832543e-04
15	10	-1.3013691e-01	5.1074214e-02	-2.0892143e-04	3.6535495e-04
15	30	-7.7774615e-02	1.7816419e-02	5.9227288e-03	-2.9717993e-05
15	50	-8.9808994e-02	2.8189577e-02	3.2041033e-03	1.9096933e-04
15	100	-8.2775974e-02	2.3982909e-02	3.8103128e-03	1.9005829e-04
15	500	-5.5353478e-02	2.1545099e-03	8.8578143e-03	-1.0428678e-04
15	1000	-2.3641070e-02	-2.2115588e-02	1.4460258e-02	-4.8270803e-04
15	5000	3.8668347e-02	-6.8920312e-02	2.5215896e-02	-1.2478985e-03
20	6	-2.6870843e-02	-2.7392640e-02	1.6457224e-02	-6.1203891e-04
20	10	-2.3393905e-02	-2.8632278e-02	1.6496182e-02	-6.2818946e-04
20	30	-1.2478324e-02	-3.3819665e-02	1.7023745e-02	-6.8905757e-04
20	50	-1.4195873e-02	-3.2968626e-02	1.6970950e-02	-6.9119069e-04
20	100	-1.4581100e-02	-3.3055789e-02	1.7057524e-02	-6.9844106e-04
20	500	3.2123656e-03	-4.9012298e-02	2.1278458e-02	-1.0175440e-03
20	1000	3.3072808e-02	-7.1569615e-02	2.6548903e-02	-1.3996529e-03
20	5000	8.4434684e-02	-1.0810294e-01	3.4681657e-02	-1.9969340e-03

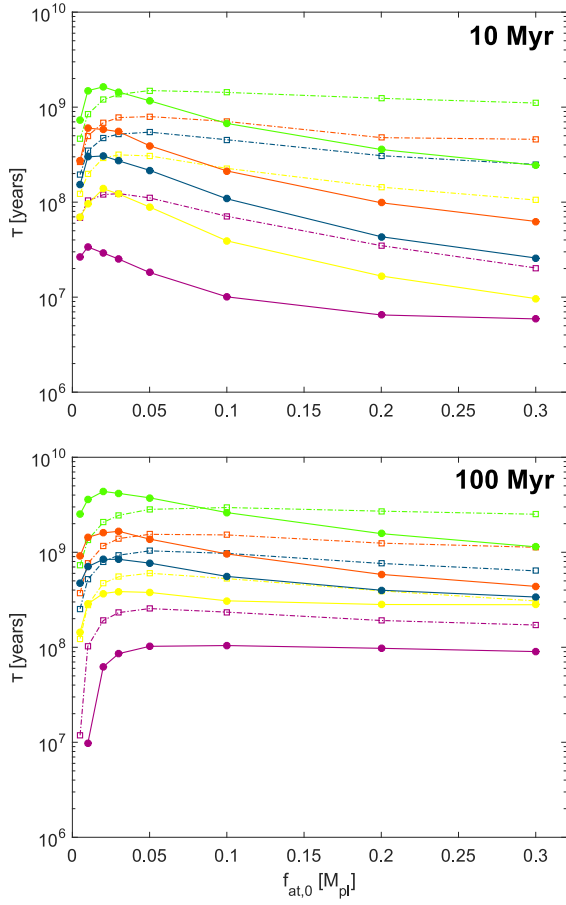


Figure 3. Instantaneous timescale for survival of atmospheres as a function of the initial atmospheric mass fraction at 10 and 100 Myr. Solid lines correspond to the hydrodynamic mass loss, and dashed lines to the energy-limited mass loss. Different colors denote different planetary core masses – from bottom to top, they are: 7.5, 10, 12.5, 15, 20 M_{\oplus} .

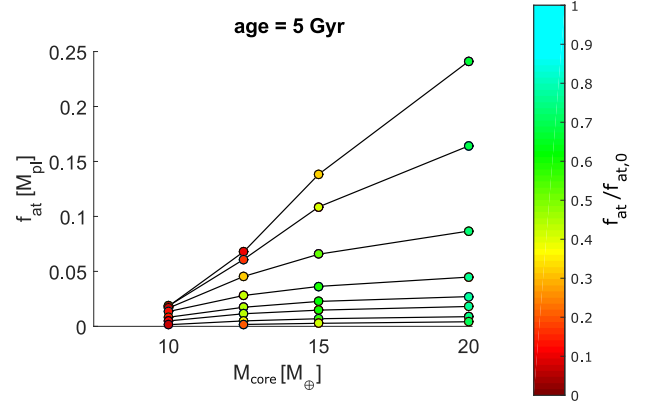


Figure 4. Atmospheric mass fractions against planetary (core) masses throughout the evolution assuming the HBA mass loss prescription. The different lines correspond to the different initial atmospheric mass fractions, from bottom to top: 0.5, 1, 2, 3, 5, 10, 20, 30%. The color code shows the fraction of initial atmosphere preserved at 5 Gyr.

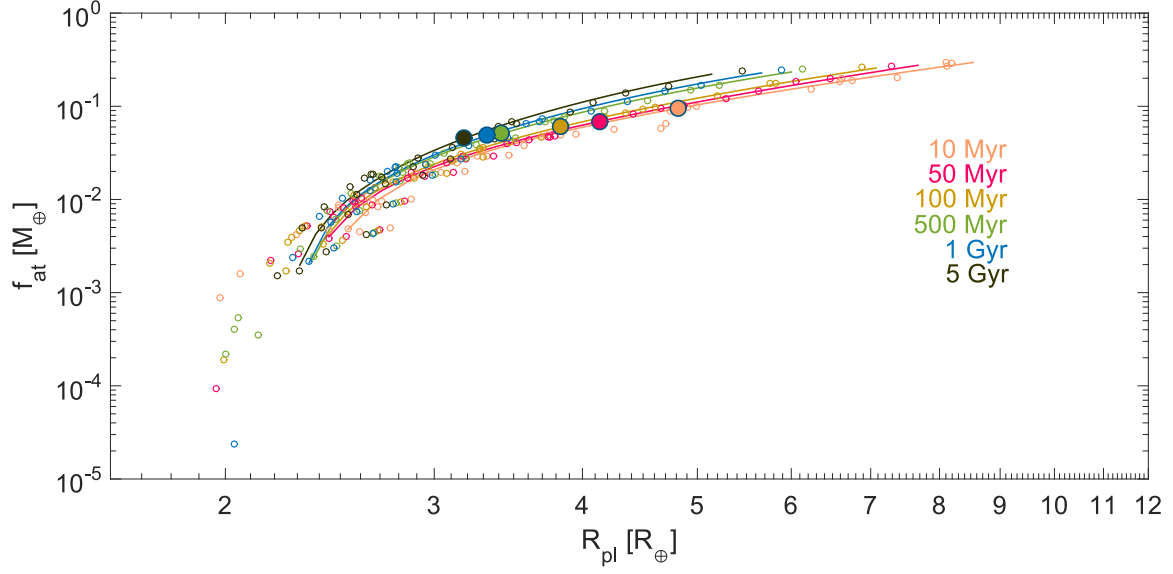


Figure 5. Evolution of the relation between f_{at} and R_{pl} for all modeled planets. Small symbols represent the instantaneous radius and atmospheric mass fraction of each individual planet at a specific age, which are color coded as given in the legend. Big circles show the evolution of the $f_{\text{at}} \times R_{\text{pl}}$ -relation with time for the planet with $12.5 M_{\oplus}$ core and $f_{\text{at},0} = 10\%$. The dashed lines are the cubic polynomial fits of the $f_{\text{at}} \times R_{\text{pl}}$ -relation for the planets with $12.5 M_{\oplus}$ core and initial atmospheric mass fractions between 0.5 and 30% at different times.

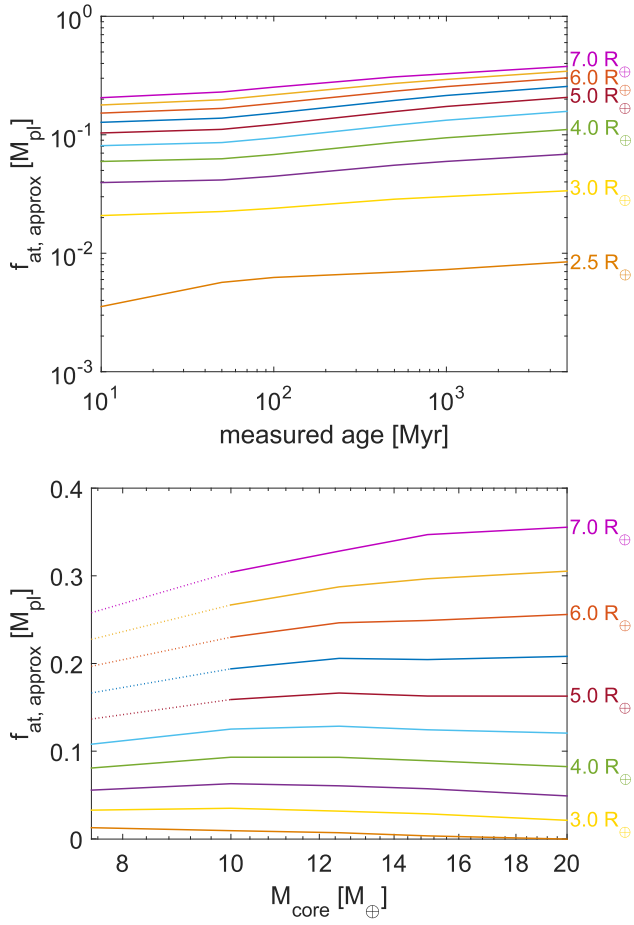


Figure 6. Atmospheric mass fraction as a function of age (of the system hosting a $12.5 M_{\oplus}$ planet, top) and core mass (bottom) obtained employing the cubic polynomial approximation of the $f_{\text{at}} \times R_{\text{pl}}$ -relation. Line colors correspond to planetary radii between 2.5 and $7 R_{\oplus}$ with a step of $0.5 R_{\oplus}$ (from bottom to top). In the bottom panel, the lines are dotted where the number of points used in the approximation is reduced (mass dependence is resolved only for ages < 500 Myr).

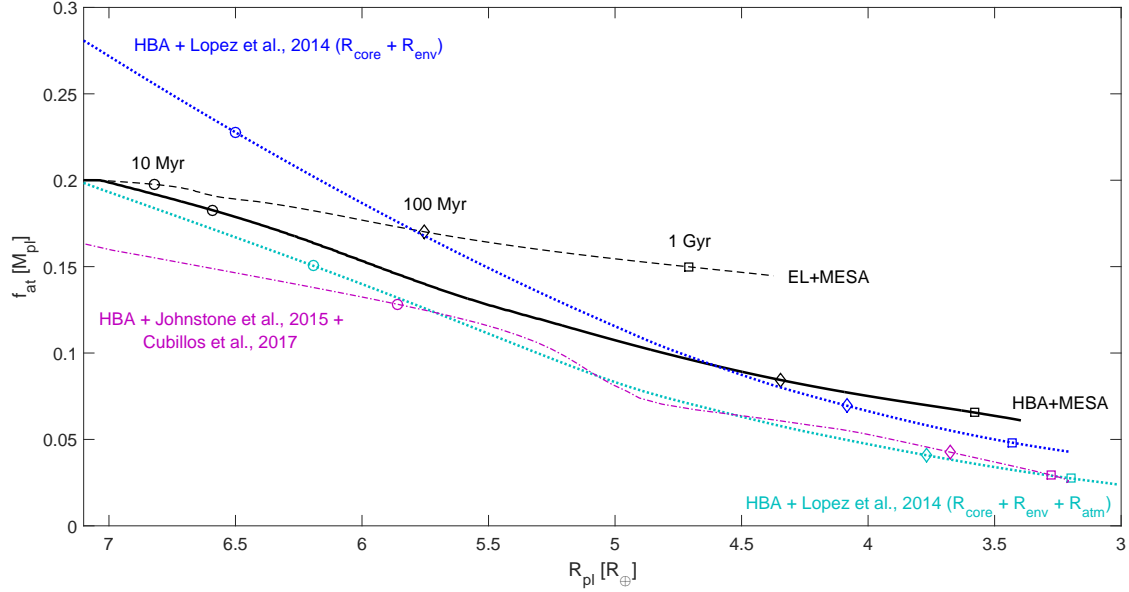


Figure 7. Relation between atmospheric mass fraction and planetary radius throughout the evolution for a planet with a core mass of $12.5 M_{\oplus}$ and 20% of initial atmospheric mass fraction. Black lines represent the result given by the self-consistent modelling of thermal evolution of the planet (MESA) and atmospheric mass loss; solid line corresponds to the hydro-based approximation (HBA) mass loss prescription and dashed line corresponds to energy-limited (EL) prescription. The colored lines represent the evolutionary tracks that do not take into account the self-consistent modelling of atmospheric escape and thermal evolution. These models employ semi-analytical approximations to define planetary radius. The light blue dotted line considers the analytical approximation of [Lopez & Fortney \(2014\)](#), the dark blue dotted line uses the same approximation, but excludes the upper radiative part of the atmosphere, and the violet dashed-dotted line shows the approximation based on [Johnstone et al. \(2015a\)](#). For these three lines, we compute at each instant the escape of the planetary atmosphere using the HBA prescription – the radius is then recalculated for the current f_{at} using the semi-analytical approximations. Because this is not self-consistent, the structure of the planet does not ‘respond’ to mass loss in the same way as in our MESA models.

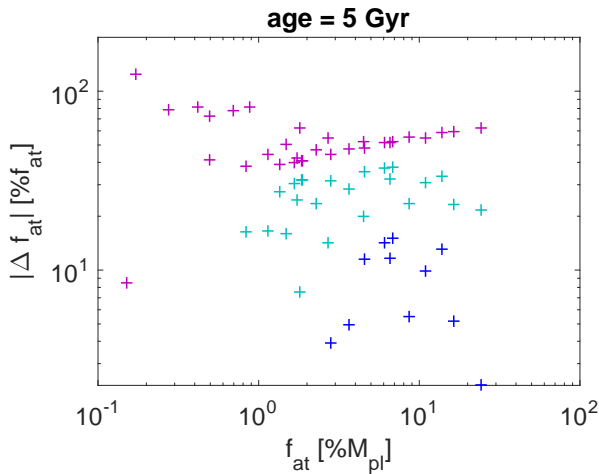


Figure 8. Relative differences between our preferred model (MESA+HD) and the three other models presented in Figure 7 at an age of 5 Gyr. As in Figure 7, light blue color corresponds to the approximation from [Lopez & Fortney \(2014\)](#), dark blue is for the same approximation, but without the upper radiative part of the atmosphere, and magenta is for estimates based on [Johnstone et al. \(2015a\)](#).

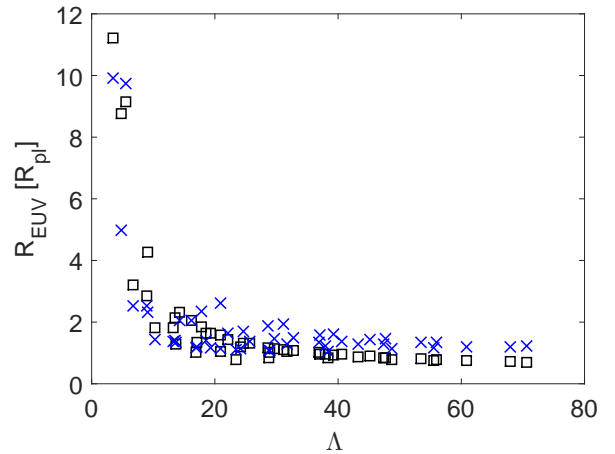


Figure A1. Effective radius of the absorption of stellar XUV radiation for the sample of planets considered in this work. Black squares represent the radii used for the energy limited approach (as given by Equation 4), and blue crosses show the R_{XUV} obtained for the same planetary parameters by interpolation within the grid of hydrodynamical models of upper atmospheres ([Kubyshkina et al. 2018a](#)).